Phase-field simulation during directional solidification of a binary alloy using adaptive finite element method

Takaki, Tomohiro

Fukuoka, Toshimichi

Tomita, Yoshihiro

(Citation)
Journal of Crystal Growth,283(1-2):263-278

(Issue Date)
2005-09

(Resource Type)
journal article

(Version)
Accepted Manuscript

(URL)
https://hdl.handle.net/20.500.14094/90000004

Phase-Field Simulation During Directional Solidification of A Binary Alloy Using Adaptive Finite Element Method

Tomohiro Takaki [a, *], Toshimichi Fukuoka [a], Yoshihiro Tomita [b]

[a] *Department of Maritime Sciences, Kobe University, Kobe, 658-0022, Japan*

[b] *Graduate School of Science and Technology, Kobe University, Kobe, 657-8501, Japan*

*Corresponding author

Tomohiro Takaki

Department of Maritime Sciences, Kobe University,

5-1-1, Fukaeminami, Higashinada, Kobe, 658-0022, Japan

Tel. : +81-78-431-4693, Fax : +81-78-431-6286

E-mail address : takaki@maritime.kobe-u.ac.jp

Abstract

We have performed phase-field simulations during directional solidification of a binary alloy. Adaptive mesh refinement techniques, in which the degrees of freedom of additional hanging nodes which occur when a quadrilateral element is refined are eliminated by matrix operations, are introduced to the finite element analysis in order to conduct the phase-field simulations efficiently. The validity of the numerical techniques presented here is ascertained by comparing the numerical results of the absolute stability limit and the onset of instability with those calculated from the Mullins–Sekerka theory and from the good linear relationship between $\log(V)$ and $\log(\lambda)$, in which the simulations under the constant concentration and temperature gradient are conducted by varying the pulling velocity. Furthermore, we examine the morphology change from cellular to dendritic structure and the relationship between $\log(\lambda)$ and $\log(G)$ for varying the temperature gradient.

PACS : 07.05.Tp; 81.30.Fb; 68.70; 68.35.J; 47.20.Hw

Keywords : A1. Computer simulation; A1. Directional solidification; A1. Crystal morphology; A1. Dendrites; A1. Interfaces; A1. Morphological stability

1. introduction

In the directional solidification of binary alloy systems, the morphological transition from the planar interface to the periodic dendritic or cellular structure is a phenomenon attracting much interest and an important problem. Therefore, experimental, theoretical, and numerical studies on directional solidification have been carried out over the past 50 years [1]. Above all, due to the rapid progress in computer technology, the computer simulation become the most powerful way to predict the morphological change at the transition growth and the characteristic shape at the steady-state growth.

In the last decade, phase-field methods have attracted considerable interest as a means of simulating microstructural development during solidification [2, 3]. The phase-field method introduces an auxiliary continuous order parameter ϕ, which takes the constant value in the solid and liquid, with a rapid transition in the vicinity of the solid-liquid interface. The main advantage of the method is that the location of the solid-liquid interface is given implicitly by the phase field. However, since fine meshes are needed to allow continuous and sharp variations of the phase field in small interface regions, considerable computer resources are required when we perform the phase-field simulations using a regular grid, particularly for a large system.

From the viewpoint of numerical calculation, we need not solve the phase-field equation in the bulk phase, because the phase field ϕ is constant inside both liquid and solid. In other words, we need only solve it in the vicinity of the interface. The region in which the phase-field equation must be solved is considerably small, since the area of the solid-liquid interface is generally much smaller than the full computational domain. Adaptive mesh techniques which use fine meshes only around the interface and coarse ones in the bulk phase, therefore, have been successfully applied to the phase-field simulation. Since the method must dynamically adapt the grid to follow the evolving interface, the adaptive method using a fixed grid is more appropriate for reducing the grid operating time and more robust than the deforming grid method often used in structural analysis. The finite difference method [4, 5], finite element method [6-10], and finite volume method [11-13] have been applied in the adaptive phase-field simulations.

Recently, the phase-field methods have also been applied to directional solidification [14-20]. The adaptive method could be more appropriate for the directional solidification problem than for the undercooling one, because a large computational domain and a long calculation time are required to evaluate the characteristics of the steady-state growth, such as primary arm spacing, after the planar initial interface becomes unstable and competitive growth occurs between dendritic or cellular arrays.

In this study, phase-field simulations during the directional solidification of a binary alloy are conducted by using the adaptive finite element method. In previous studies for the adaptive phase-field simulation using the finite element method, a triangular [6, 7] or a quadrilateral element with an additional triangle element to connect the extra node [8-10] has been used. Here, we introduce the adaptive finite element method only using an isoparametric quadrilateral element, in which the degree of freedom for the extra hanging node which occurs when an element is split into four child elements is eliminated by conducting the matrix operation. The simulations are performed under similar conditions to those of Boettinger [14] and Lan [15], and the effects of the pulling velocity and the temperature gradient on the interface morphology and the primary arm spacing are examined.

2. Simulation Method

2.1 Phase-field equations

The thermodynamically consistent phase-field model for a binary alloy based on the entropy functional is adopted here [21, 22]. We briefly summarize the used phase-field model in this section [21, 22]. In the present simulations during directional solidification, the temperature gradient is assumed to be constant. The phase-field equation and concentration field equation, therefore, must be solved numerically. Considering the effects of anisotropy and noise, the equations in a two-dimensional problem are as follows:

$$\frac{\partial \phi}{\partial t} = M_\phi \left[-\frac{\partial}{\partial x}\left(\varepsilon \frac{\partial \varepsilon}{\partial \theta}\frac{\partial \phi}{\partial y}\right) + \frac{\partial}{\partial y}\left(\varepsilon \frac{\partial \varepsilon}{\partial \theta}\frac{\partial \phi}{\partial x}\right) + \nabla \cdot \left(\varepsilon^2 \nabla \phi\right) - \left(1 - 16 a \chi g(\phi)\right)\left\{(1-c)H^A(\phi,T) + cH^B(\phi,T)\right\}\right] \tag{1}$$

$$\frac{\partial c}{\partial t} = -\nabla \cdot \left\{ D_c c(1-c)\frac{v_m}{R}\left[H^A(\phi,T) - H^B(\phi,T)\right]\nabla \phi - D_c \nabla c \right\} \tag{2}$$

where ϕ is a phase field taking a value of 0 in the liquid and 1 in the solid, and c is the concentration of solute, T is the temperature, t is the time, ε represents gradient corrections to the entropy density, a is the amplitude of the fluctuations, χ is a random number distributed uniformly in the interval [-1, 1], v_m is the molar volume, and R is the gas constant.

The interface anisotropy is taken into consideration by using the following equation.

$$\varepsilon(\theta) = \bar{\varepsilon}\{1 + \gamma \cos(k\theta)\} \tag{3}$$

Here, $\bar{\varepsilon}$ is a constant related to the surface energy σ and interface thickness h, γ is the strength of anisotropy, k is the anisotropy mode, and θ is the angle between the interface normal and the x-axis.

$H^A(\phi, T)$ and $H^B(\phi, T)$ in Eqs.(1) and (2) are defined by

$$H^{A,B}(\phi,T) = G^{A,B'}(\phi) + p'(\phi) L^{A,B}\left(\frac{T - T_m^{A,B}}{T T_m^{A,B}}\right) \tag{4}$$

where the prime denotes a derivative with respect to ϕ. $G^{A,B}(\phi) = W^{A,B} g(\phi)$. $g(\phi) = \phi^2(1-\phi)^2$ is the double-well potential. $p(\phi) = \phi^3(10 - 15\phi + 6\phi^2)$ is a monotonically increasing function which satisfies $p(0) = 0$, $p(1) = 1$, and $p'(\phi) = 30\, g(\phi)$. $T_m^{A,B}$ and $L^{A,B}$ are the melting point and latent heat of fusion of pure A and B. Here, the superscripts A and B represent solvent and solute, respectively.

It is assumed that M_ϕ depends on the composition and has the form $M_\phi = (1-c)\, M_\phi^A + c\, M_\phi^B$. The diffusion coefficient D_c is postulated as a function of the phase field, $D_c = D_l + p(\phi)(D_s - D_l)$, where D_s and D_l are the classical diffusion coefficients in the solid and liquid, respectively.

By assuming the equilibrium condition and the steady-state interface growth in one dimension for pure A and B, M_ϕ^A, M_ϕ^B, W^A, W^B, and, $\bar{\varepsilon}$ are related to the measurable quantities as follows [21]:

$$M_\phi^{A,B} = \frac{\mu^{A,B}\left(T_m^{A,B}\right)^2 b}{3 L^{A,B} h^{A,B}}, \quad W^{A,B} = \frac{6\sigma^{A,B} b}{T_m^{A,B} h^{A,B}}, \quad \bar{\varepsilon}^2 = \frac{3\sigma^{A,B} h^{A,B}}{T_m^{A,B} b} \tag{5}$$

where $\mu^{A,B}$, $\sigma^{A,B}$, and $h^{A,B}$ are the kinetic coefficient, the surface energy, and the interface thickness of pure A and B, respectively. From the equation of $\bar{\varepsilon}$ in Eq.(5), h^B is determined using h^A.

$$h^B = \frac{\sigma^A}{\sigma^B}\frac{T_m^B}{T_m^A} h^A \tag{6}$$

Assuming that the interface region is $\xi < \phi < 1-\xi$, we obtain

$$b = 2\tanh^{-1}(1-2\xi) \tag{7}$$

Here, ξ is set to be 0.1, so that b reduces to 2.20. Although the definition of the interface thickness is different from one of Ref.[21], the parameters of Eq.(5) reduce to the almost same values with those of Ref.[21] by the above choice of ξ and using $h^A = 6dx$ where dx is the minimum mesh size.

2.2 Finite element method

Space is discretized using the finite element method. Finite element approximation of the weak forms of Eqs.(1) and (2) results in the following finite element equations:

Phase-field

$$\left[K_\phi^1\right]\left\{\frac{\partial \phi}{\partial t}\right\} + \left[K_\phi^2\right]\{\phi\} = \{f_\phi\} \tag{8}$$

$$\left[K_\phi^1\right] = \int_A \frac{1}{M_\phi}\varphi_N \varphi_M \, dA \tag{9}$$

$$\left[K_\phi^2\right] = \int_A \left\{ -\varepsilon \frac{\partial \varepsilon}{\partial \theta}\left(\frac{\partial \varphi_N}{\partial y}\frac{\partial \varphi_M}{\partial x} - \frac{\partial \varphi_N}{\partial x}\frac{\partial \varphi_M}{\partial y} \right) + \varepsilon^2 \left(\frac{\partial \varphi_N}{\partial x}\frac{\partial \varphi_M}{\partial x} + \frac{\partial \varphi_N}{\partial y}\frac{\partial \varphi_M}{\partial y} \right) \right\} dA \tag{10}$$

$$\{f_\phi\} = -\int_A \left(1 - 16a\chi g(\phi)\right)\left\{(1-c)H^A(\phi,T) + cH^B(\phi,T)\right\}\varphi_M \, dA \tag{11}$$

Concentration field

$$\left[K_c^1\right]\left\{\frac{\partial c}{\partial t}\right\} + \left[K_c^2\right]\{c\} = \{f_c\} \tag{12}$$

$$\left[K_c^1\right] = \int_A \varphi_N \varphi_M \, dA \tag{13}$$

$$\left[K_c^2\right] = \int_A D_c \left(\frac{\partial \varphi_N}{\partial x}\frac{\partial \varphi_M}{\partial x} + \frac{\partial \varphi_N}{\partial y}\frac{\partial \varphi_M}{\partial y} \right) dA \tag{14}$$

$$\{f_c\} = \int_A \left\{ D_c c(1-c)\frac{v_m}{R}\left(\frac{\partial \varphi_N}{\partial x}\frac{\partial \varphi_M}{\partial x} + \frac{\partial \varphi_N}{\partial y}\frac{\partial \varphi_M}{\partial y} \right)\left[\left(H^A(\phi,T) - H^B(\phi,T)\right)\phi_N + \Gamma(\phi,T)T_N\right] \right\} dA \tag{15}$$

where the phase-field ϕ and the concentration c at any point in the element can be defined in terms of the nodal values ϕ_i and c_i at node i and the shape function φ as $\phi = \varphi_i\phi_i$ and $c = \varphi_i c_i$, respectively. The isoparametric quadrilateral element is used here.

The Crank-Nicolson scheme is used for time discretization. The phase-field ϕ^{t+dt} and the concentration c^{t+dt} at time $t+dt$, therefore, can be obtained by solving the following equations.

$$\left(\frac{1}{dt}\left[K_\phi^1\right] + \frac{1}{2}\left[K_\phi^2\right]\right)\{\phi^{t+dt}\} = \left(\frac{1}{dt}\left[K_\phi^1\right] - \frac{1}{2}\left[K_\phi^2\right]\right)\{\phi^t\} + \{f_\phi\} \tag{16}$$

$$\left(\frac{1}{dt}\left[K_c^1\right] + \frac{1}{2}\left[K_c^2\right]\right)\{c^{t+dt}\} = \left(\frac{1}{dt}\left[K_c^1\right] - \frac{1}{2}\left[K_c^2\right]\right)\{c^t\} + \{f_c\} \tag{17}$$

Here, dt indicates the time increment. $\{f_\phi\}$ and $\{f_c\}$ are calculated using the values of ϕ^t and c^t at time t. The matrix on the left-hand side of Eq.(16) is nonsymmetric, while the matrix of Eq.(17) is symmetric.

2.3 Adaptive mesh technique

The element is refined by splitting into four child elements as shown in Fig.1. Some extra nodes are, then, necessarily created. If the refinement levels of two neighboring elements are different from each other, a new node appears on the side of a larger element. The new node is referred to as a hanging node in this study. In Fig.1, node 10 is the hanging node.

As a method for handling these extra hanging nodes, a connecting element with triangle elements called bridge elements has been introduced in Refs. [8-10]. In this study, we adopt the method in which the degrees of freedom of the hanging nodes are eliminated by conducting matrix operations. The procedures of the method are explained in detail by using the mesh pattern on the lower side of Fig.1.

The following constraint equation must be satisfied for node 10.

$$\phi_{10} = \frac{1}{2}\left(\phi_2 + \phi_5\right) \tag{18}$$

Equation (16) for element 2 in the mesh pattern on the lower side of Fig.1 becomes as

$$\begin{bmatrix} a_{11} & a_{12} & a_{13} & a_{14} \\ a_{21} & a_{22} & a_{23} & a_{24} \\ a_{31} & a_{32} & a_{33} & a_{34} \\ a_{41} & a_{42} & a_{43} & a_{44} \end{bmatrix} \begin{Bmatrix} \phi_2^{\,t+dt} \\ \phi_7^{\,t+dt} \\ \phi_{11}^{\,t+dt} \\ \phi_{10}^{\,t+dt} \end{Bmatrix} = \begin{bmatrix} b_{11} & b_{12} & b_{13} & b_{14} \\ b_{21} & b_{22} & b_{23} & b_{24} \\ b_{31} & b_{32} & b_{33} & b_{34} \\ b_{41} & b_{42} & b_{43} & b_{44} \end{bmatrix} \begin{Bmatrix} \phi_2^{\,t} \\ \phi_7^{\,t} \\ \phi_{11}^{\,t} \\ \phi_{10}^{\,t} \end{Bmatrix} + \begin{Bmatrix} f_2 \\ f_7 \\ f_{11} \\ f_{10} \end{Bmatrix} \tag{19}$$

where a_{ij} and b_{ij} are the components of matrices $\left(\frac{1}{dt}\left[K_\phi^1\right] + \frac{1}{2}\left[K_\phi^2\right]\right)$ and $\left(\frac{1}{dt}\left[K_\phi^1\right] - \frac{1}{2}\left[K_\phi^2\right]\right)$ in Eq.(16), respectively, and the subscripts i and j represent the local node numbers in the element. Substituting Eq.(18) into Eq.(19) gives the following equation.

$$\begin{bmatrix} a_{11}+a_{14}/2 & a_{12} & a_{13} & a_{14}/2 \\ a_{21}+a_{24}/2 & a_{22} & a_{23} & a_{24}/2 \\ a_{31}+a_{34}/2 & a_{32} & a_{33} & a_{34}/2 \\ a_{41}+a_{44}/2 & a_{42} & a_{43} & a_{44}/2 \end{bmatrix} \begin{Bmatrix} \phi_2^{\,t+dt} \\ \phi_7^{\,t+dt} \\ \phi_{11}^{\,t+dt} \\ \phi_5^{\,t+dt} \end{Bmatrix} = \begin{bmatrix} b_{11}+b_{14}/2 & b_{12} & b_{13} & b_{14}/2 \\ b_{21}+b_{24}/2 & b_{22} & b_{23} & b_{24}/2 \\ b_{31}+b_{34}/2 & b_{32} & b_{33} & b_{34}/2 \\ b_{41}+b_{44}/2 & b_{42} & b_{43} & b_{44}/2 \end{bmatrix} \begin{Bmatrix} \phi_2^{\,t} \\ \phi_7^{\,t} \\ \phi_{11}^{\,t} \\ \phi_5^{\,t} \end{Bmatrix} + \begin{Bmatrix} f_2 \\ f_7 \\ f_{11} \\ f_{10} \end{Bmatrix} \tag{20}$$

Here, the connectivity {2, 7, 11, 10} of element 2 is changed to {2, 7, 11, 5}. The value of f_{10} in Eq.(20) is added into the component corresponding to node 5 of the global right-hand side vector, although f_{10} is calculated using the value of node 10 at time t.

The above matrix operation is repeated for all elements with the hanging node. In the example of the mesh pattern on the lower side of Fig.1, the element corresponds to elements 2 and 4. Although the procedure is explained only for the phase field, the same operation is performed for the concentration field. The linear equations are solved by using the element-by-element preconditioned bi-conjugate gradient method [23], since the matrix of the left-hand side of Eq.(17) also becomes nonsymmetric under the above matrix operations. This method can be introduced to the original finite element code using regular grid much easily than one using bridge element [8-10].

Since the adaptive method must dynamically adapt the grid to follow the interface evolving during solidification, the refinement and coarsening as shown in Fig.1 are repeated during the simulation. If

refinement is desired for an element, the element is split into four child elements and some extra nodes are yielded. Coarsening consists of fusing the four child elements back into the parent element, and thus some nodes are eliminated. In order to perform the continuous refinement and coarsening operations efficiently, our code was developed based on the concept of the quadtree data structure [8].

Figure 2 illustrates an example mesh and a quadtree element data structure for the mesh. Four levels of refinement, from level 0 to level 3, are used in Fig.2. The finite element equations are solved for the elements with a number enclosed in a circle, which are called active elements here. The active elements locate at the terminal branches of the quadtree. The other elements which are not active elements must also have some information for the refinement and coarsening. Numbers 1 through 4 enclosed in a square on the quadtree indicate the local element numbers in their parent element. All elements enclosed in a square contain the following information: connectivity, four neighboring elements with identical refinement levels, hanging nodes on the four edges, four child element numbers, a parent element number and a local element number in the parent element, a flag indicating whether the element is an active element or not, and an active element number if the element is active.

The grid is adapted dynamically based on an error estimator that utilizes information from both the phase field ϕ and concentration field c. We impose the restriction that any two neighboring quadrilateral elements may not be separated by more than one level of refinement. For example, therefore, if element 5 in Fig.2 is judged as being refined, elements 1 and 2 neighboring to element 5 must be also refined. The coarsening can be performed only if all four elements sharing the same parent element are judged as being coarsened.

2.4 Numerical conditions

The directional solidification simulations of Ni-40at.%Cu are performed under similar conditions to those in Refs. [14, 15]. The following physical data, phase-field parameters, and other conditions are used in the present simulations: $T_m^{A,B} = 1728$ and 1358 K, $L^{A,B} = 2350\times10^6$ and 1728×10^6 J/m^3, $v_m^{A,B} = 7.0\times10^{-6}$ and 7.8×10^{-6} m^3/mol, $D_l^{A,B} = 1.0\times10^{-9}$ m^2/s, $D_s^{A,B} = 1.0\times10^{-13}$ m^2/s, $\sigma^{A,B} = 0.37$ and 0.29 J/m^2, $\mu^{A,B} =$ 0.0033 and 0.0039 m/Ks, $h^{A,B} = 0.300$ (= $6dx$) and 0.301 μm, $W^{A,B} = 9409$ and 9359 J/Km^3, $M^{A,B} = 10.24$ and 10.13 m^{3}K/sJ, $\bar{\varepsilon} = 9.365\times10^{-6}$ (J/mK)$^{0.5}$, $\gamma = 0.04$, $k = 4$, $a = 0.4$, $dx = 0.05$ μm, and $dt = 1$ μs, in which the superscripts A and B denote Ni and Cu, respectively. In order to compare the present results with previous ones [14, 15], we assume the kinetic coefficients so as to be $M_\phi \varepsilon^2 \approx D_c$. These values are the same as the ones used by previous papers [14, 15]. The values are smaller than the realistic values, $\mu \approx 2$ m/Ks, and allow using large time increment dt. It is, however, observed that the kinetic coefficient has less effect on the steady-state interface morphology, by conducting simulations using some values of the kinetic coefficients.

Figure 3 shows the computational domain, boundary conditions and initial conditions. We have attempted to introduce the advection term into Eqs.(1) and (2) in order to simulate the directional solidification process corresponding to the in-situ observation [15]. However, the solutions diverged in the region located immediately behind the interface in which the diffusion coefficient is relatively small, $D_c \approx D_s$. An extremely small time step was needed to achieve the stability of the solutions. It is well known that the numerical solutions of the advection equation, which include the spatial first-order

derivative, become unstable easily. In order to make the most of the advantage of the implicit scheme employed here, we use the long computational domain and the method that reduces the temperature of all domains *GVdt* at every time step, instead of introducing the advection term. When we solve the problem in which the thermal profile is dynamically changed, we have only to use longer computational domain with coarse meshes. Here, the rectangle meshes having long axis in thermal gradient direction are possible to use in order to conduct the adaptive operation more efficiently. On the other hands, the method which increases the computational domain with the progress of the simulation, which is in contrast with "cut off operation" described in later section, is also efficient for non-isothermal problem. For non-isothermal problem, however, not only the large computational domain but also many time steps are required as pointed out by Lan and Chang [15] so that a phase-field model with new concept such as anti-trapping [24] which can use a large interface thickness is desired. The initial planar interface is placed at the position 1.6 μm from the left-hand side of the computational domain. The initial interface position corresponds to the liquidus temperature T_i = 1597.4 K for the concentration c = 0.4 at. frac.. The initial conditions for the phase field and the concentration field are taken as step functions. The concentration is initially set as $c = c_s$ =0.338 in solid phase and $c = c_l$ = 0.4 in liquid phase, in which c_s and c_l are the equilibrium flat interface concentrations of the solid and liquid sides, respectively. The equilibrium partition coefficient is calculated as $k = c_s/c_l$ = 0.845. The temperature distribution $T = T_i + G$(x-1.6) is assumed at the initial conditions so as to obtain the constant gradient G. In this study, the effects of the pulling velocity V and the temperature gradient G on the interface morphology around the dendrite or cell tip and the primary arm spacing are examined. The primary arm spacing is affected by the width of the computational domain. The computational domain is, therefore, determined such that it yields more than ten periodic dendritic or cellular structures. Eight levels of refinement which is Level 0 through Level 7 are used, so that the element size of level 0 becomes $dx_0 = 2^7 \times dx$ = 6.4 μm, in which dx = 0.05 μm is the element size of level 7. The refinement is performed when ($0.001 \le \phi_{ave} \le 0.9$) or ($|\nabla c_{ave}| \ge 0.01$, $\phi_{ave} < 0.001$ and refinement level < 7) , where ϕ_{ave} is the average value of four nodal values ϕ_i in an element and ∇c_{ave} is the average value of ∇c at four Gauss points in an element. In present simulations, the computational time is proportional to the number of the active elements. Therefore, in order to reduce the number of the active elements we set above refinement criteria for the concentration field, since the solute boundary layer is wider than the interface region and the gradient of the concentration distribution is smaller than that of the phase field.

3. Numerical results

3.1 Interface morphology

Figure 4 illustrates the time evolutions of the interface (ϕ = 0.5) and the concentration field for the conditions of temperature gradient G = 0.134375 (=2.15/16) K/μm, pulling velocity V = 0.0025 m/s, and computational domain size DX = 288.0 μm and DY = 115.2 μm. The quarter regions from the left-hand side are demonstrated in Fig.4 (a) to (d) , and the full regions in Fig.4 (e) to (g). As shown in Fig.4 (e), (f), and (g), the computational domain is reduced by increasing the number of time steps for the purpose of reducing the computational cost, because we are not interested in characteristic shapes such as the

mushy zone depth but in the interface morphology around the dendrite or cell tip and the primary arm spacing. Figure 5 shows the variations of the tip velocity of the cell identified with an arrow in Fig.4 (g) and the total number of active elements. The left-hand side of the domain is cut off every 2560 steps (= $dx_0/V/dt$) from the 64000th step. The number of active elements, therefore, fluctuate from the 64000th step. The time which starts the cutting off operation is determined by performing the preliminary calculations using the computational domain with the smaller width. The time step dt is set to be 1 μs, so that the time is same as the step number. The interface growth process can be divided into three stages as seen in Figs.4 and 5. First, the interface remains in the initial position for a certain period (Fig.4 (a)). At about the 40000th step, the planar interface becomes unstable (Fig.4 (b)). Initially, a cellular pattern develops and then goes through a stage of competitive growth (Fig.4 (c)). The cellular structure subsequently transforms into a dendritic structure (Fig.4 (d), (e), and (f)). During these steps from Fig.4 (b) through Fig.4 (e), the tip grows at an accelerated pace, as shown in Fig.5 (a). After the tip velocity achieves to maximum value, it become slowly and finally approaches to the pulling velocity V = 0.0025 m/s. Figure 4 (g) shows a stage of steady-state growth. In Fig.4 (e) and (f), close-up views of mesh division around the tip and at the interdendritic region are also illustrated. It is found that the meshes satisfactorily adapt to the interface and the solute boundary layer.

3.2 Effects of velocity

To confirm the validity of the numerical techniques presented in this study, we examine the absolute stability limit, the onset of instability, and the relationship between the velocity and the primary arm spacing by varying the pulling velocity under the constant gradient G = 2.15 K/μm and the constant concentration c = 0.4 at. frac.. The pulling velocity V is varied to values such as 0.04, 0.03, 0.02, 0.01, 0.005, 0.0025, 0.00125, 0.000625, 0.0003125, 0.00015625, and 0.000078125 m/s. Table 1 shows the length of the computational domain DX, the width of the domain DY, the total time t_{total}, the number of the dendritic or cellular structures yielded at the steady-state growth N, and the calculated average primary arm spacing λ for each pulling velocity V. This work is similar to studies by Boettinger [14] and Lan [15].

Figure 6 shows the steady-state cellular structures at time t_{total} for the velocities from 0.02 to 0.0003125 m/s. A part of the all interface is illustrated as for V = 0.0003125 m/s. For the velocities of 0.03 and 0.04 m/s, the planar interface is observed to be in the stage of steady-state growth. It is, therefore, considered that the absolute stability limit is between 0.02 and 0.03 m/s. At lower speeds, the interface for V = 0.000078125 m/s remains flat throughout the simulation in which the calculations of 1.92 million steps are conducted using very long computational domain. The onset of instability may, therefore, lie between V = 0.00015625 and 0.000078125 m/s. Regarding V = 0.00015625 m/s, the long time scale morphological dynamics is observed, because it is near the onset of instability from planner to cellular structures [16, 25, 26]. This problem needs very long time. We, therefore, use the long computational domain and the long calculating time for V = 0.00015625 m/s comparing to the lower pulling velocity, as indicated in Table.1. Figure 7 illustrates the interface morphologies every 48000 steps from 480000th step to 960000th step. The cell splitting or cell coalescence is observed. The wavelength of each cell varies during the simulation, and the interface never reaches steady-state growth. These phenomenon observed here agree well with those of the previous studies [25, 26]. The detail studies of morphological evolution

around this lower MS-loop boundary have been performed experimentally and numerically in Ref. [27]. From the results of Ref. [27], it is concluded that the system never reaches stable morphology in the absence of an initial perturbation. This result is similar to the present ones, because the present simulations start from the planer initial interface.

Figure 8 (a) indicates the relationship between the velocity V and the numerical results for the average primary arm spacing λ, for the velocities in the range from 0.02 to 0.00015625 m/s, together with the MS-loop calculated using the Mullins–Sekerka theory [28]. The average primary arm spacing λ is defined as the width of the computational domain DY divided by the number of cellular structures yielded in the steady-state growth N. The inner side line in Fig.8 (a) is a MS-loop calculated using a velocity dependent partition coefficient k_v. Value of k_v is obtained by fitting the equation $k_v = (k+V/V_D)/(1+V/V_D)$ to the numerical results as shown in Fig.8 (b) [14, 15]. The numerical results of the absolute stability limit and the onset of instability are in good agreement with the MS-loop calculated using k_v. The tip radius is decreased with increasing the velocity as shown in Fig.6. The mesh size dx = 0.005 μm seems to be insufficient for high velocities, because a good linear relationship between log(V) and log(λ) cannot be observed at V = 0.005 m/s and above. The numerical results obtained using dx = 0.025 μm, which is half the size of the original dx = 0.05 μm and reduce to half interface thickness, are plotted using open triangles for V = 0.02, 0.01, and 0.005 m/s. These results using the mesh size dx = 0.025 μm and the results from 0.0025 m/s to 0.0003125 m/s show a good linear relationship, in which the scaling law $V\lambda^2 = const$ is approximated. We can see the better linearity between log(V) and log(λ) than the results of Refs.[14, 15]. The average primary arm spacing for V = 0.00015625 m/s is considerably small comparing to the value predicted by the scaling low. This result also agrees well with the previous study [25, 26]. As the concentration profile schematically illustrated in Fig.8 (b), the present mesh size induces solute trapping at the interface. When we reduce the mesh size, the steady-state interface morphologies are changed in the range of relatively high pulling velocities, such as V = 0.02, 0.01, and 0.005 m/s, as shown in Fig.8 (a). In the lower velocity regions, however, we cannot observe the morphological changes at the steady-state, when using smaller mesh size. To evaluate the phenomena including the solute trapping more quantitatively, a new phase-field model, with a technique such as anti-trapping proposed by Karma [24], is desired.

3.3 Effects of temperature gradient

The morphology change from cellular to dendritic structure and the primary arm spacing λ in the steady-state growth are evaluated by varying the temperature gradient G. The simulations are conducted under the conditions that V = 0.0025 m/s and G = 2.15, 1.075, 0.5375, 0.26875, 0.134375, and 0.0671875 K/μm. The numerical conditions and results are shown in Table.2. It is well known that the tip radius is independent of the amount of G, from a previous study [29]. The same mesh resolutions are, therefore, required for any value of G in the case with a constant value of V. Figure 9 illustrates the steady-state interface morphology near the cell or dendrite tip. Figure 9 (a) and (e) are identical to Fig.6 (d) and Fig.4 (g), respectively. The dendritic structures are observed in the smaller G. We can efficiently simulate the dendritic structures by using both the adaptive mesh techniques and the cutting off operations of the computational domain, although the total interface region of the dendrite becomes much larger comparing

to one of cellular structure. Figure 10 shows the plot of the temperature gradient G and the average primary arm spacing λ. A good linear relationship between $\log(\lambda)$ and $\log(G)$ is observed. Fitting the equation $\lambda = const. \times G^{-\alpha}$ to the numerical results, $\alpha = 0.52$ is obtained. The value of α is known to be 0.5 from previous theoretical studies [29]. The present result agrees well with one of the previous studies.

4. Conclusions

Phase-field simulations during directional solidification of a binary alloy are performed by using the adaptive finite element method, where the isoparametric quadrilateral element is used and the degree of freedom of the extra hanging nodes which occur during refinement is eliminated by matrix operations. This adaptive scheme can be introduced to the original finite element code with regular mesh relatively easily. The interface morphology around the dendrite or cell tip and the primary arm spacing are examined by varying the pulling velocity and the temperature gradient. The numerical results of the absolute stability limit and the onset of instability agree well with the MS-loop considering the velocity dependent partition coefficient. The plots of primary arm spacing and velocity and temperature gradient shows good linear relationships, and the relations reasonably agree well with the previous studies. The denrite, deep cell, and shallow cell with long time scale morphology are efficiently simulated using both the adaptive mesh techniques and the cutting off operations of the computational domain.

Acknowledgements

The authors would like to thank Dr. Kenichi Tsubota in Tohoku University for valuable comments about the solving method of the linear equations.

References

[1] D. T. J. Hurle, Hnad book of crystal growth 1b, North-Holland, 1993.

[2] G. Caginalp, Arch. Rat. Mech. Anal, 92 (1986) 205.

[3] R. Kobayashi, Physica D 63 (1993) 410.

[4] R. J. Braun, B. T. Murray, J. Soto Jr, Modelling Simul. Mater. Sci. Eng. 5 (1997) 365.

[5] R. J. Braun, B. T. Murray, J. Crystal Growth 174 (1997) 41.

[6] R. Tonhardt, G. Amberg, J. Crystal Growth 194 (1998) 406.

[7] R. Tonhardt, G. Amberg, J. Crystal Growth 213 (2000) 161.

[8] N. Palle, J. A. Dantzig, Metall. Mater. Trans. 27A (1996) 707.

[9] N. Provatas, N. Goldenfeld, J. Dantzig, J. Computational Physics 148 (1999) 265.

[10] N. Provatas, N. Goldefeld, J. Dantzig, Phys. Rev. Lett. 80 (1998) 3308.

[11] C. W. Lan, C. C. Liu, M. Hsu, J. Computational Physics 178 (2002) 464.

[12] C. W. Lan, C. M. Hsu, C. C. Liu, J. Crystal Growth, 241 (2002) 379-386.

[13] C. W. Lan, Y. C. Chang, C. J. Shih, Acta Mater. 51 (2003) 1857.

[14] W. J. Boettinger, J. A. Warren, J. Crystal Growth 200 (1999) 583.

[15] C. W. Lan, Y. C. Chang, J. Crystal Growth 250 (2003) 525.

[16] C. W. Lan , C. J. Shih and W. T. Hsu, J. Crystal Growth 264 (2004) 379.

[17] H. –J. Diepers, D. Ma, I. Steinbach, J. Crystal Growth 237-239 (2002) 149.

[18] Zhiqiang Bi, R. F. Sekerka, J. Crystal Growth 237-239 (2002) 138.

[19] N. Provatas, Q. Wang, M. Haataja, M. Grant., Phys. Rev. Lett. 91 (2003) 155502-1.

[20] T. Takaki, T. Fukuoka, Y. Tomita, Trans. JSME A (Japanese) 70 (2004) 128.

[21] J. A. Warren, W. J. Boettinger, Acta. Metal. Mater. 43 (1995) 689.

[22] I. Loginova, G. Amberg, J. Agren, Acta. Mater. 49 (2001) 573.

[23] T. J. R. Hughes, R. M. Ferencz, Compt. Mehods Appl. Mech. & Eng. 61 (1987) 215.

[24] A. Karma, Phys. Rev. Lett., 87 (2001) 115701-1.

[25] J. T. C. Lee, R. A. Brown, Phys. Rev.B 47 (1993) 4937.

[26] K. Tsiveriotis, R. A. Brown, Phys. Rev.B 49 (1994) 12724.

[27] W. Losert, D. A. Stillman, H. Z. Cummins, P. Kopczynski, W. –J. Rappel, A. Karma, Phys. Rev. E, 58 (1998) 7492.

[28] W. W. Mullins, R. F. Sekerka, J. Applied Physics 35 (1964) 444.

[29] M. Gündüz, E. Çadırlı, , Mater. Sci. Eng. A327 (2002) 167.

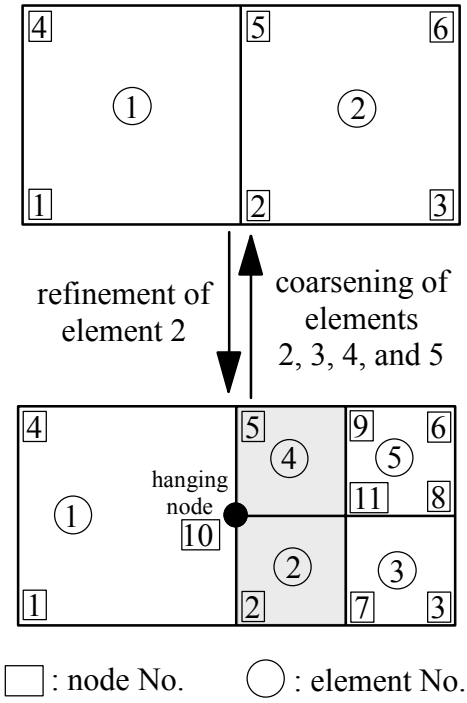

Fig.1 Element refinement and coarsening, and hanging node.

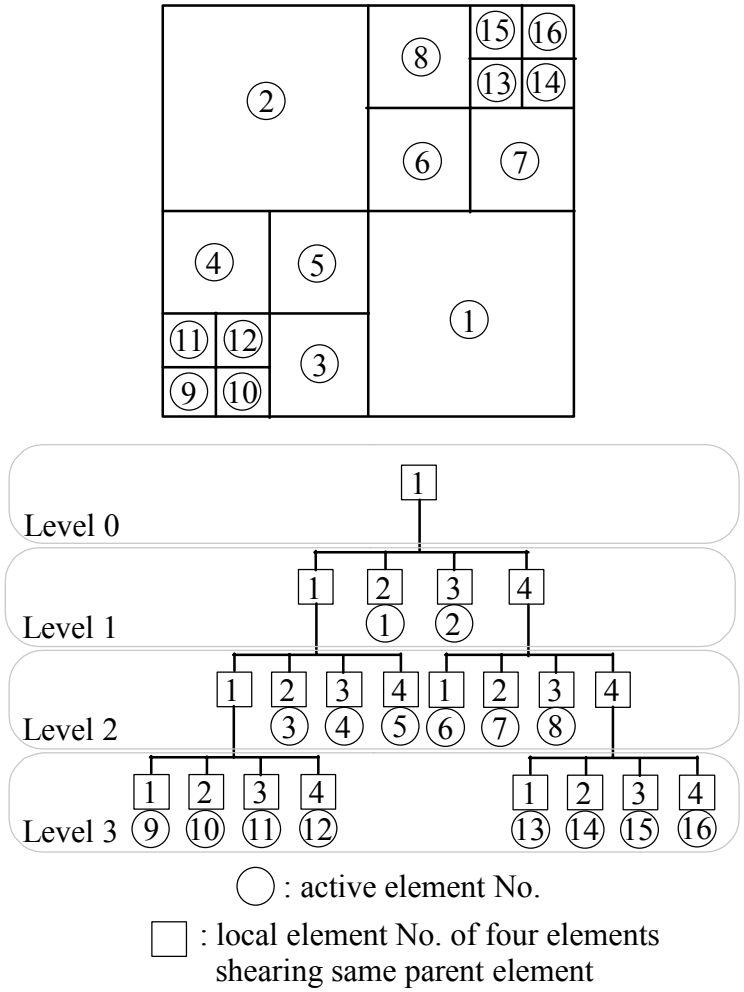

Fig.2 Example mesh and its quadtree element data structure.

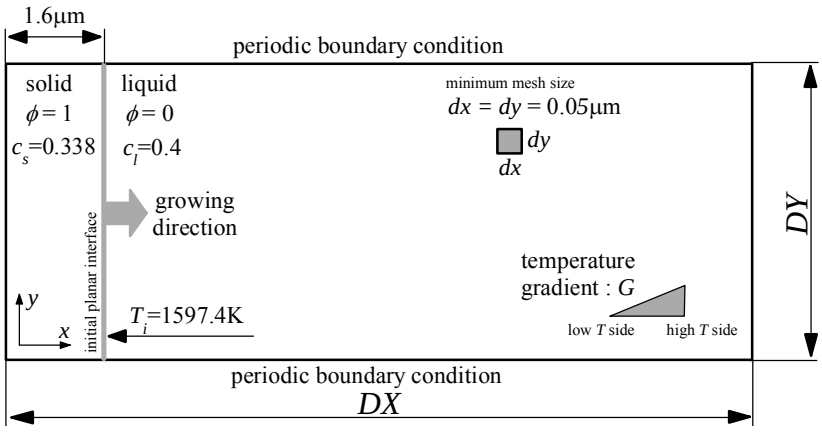

Fig.3 Computational model.

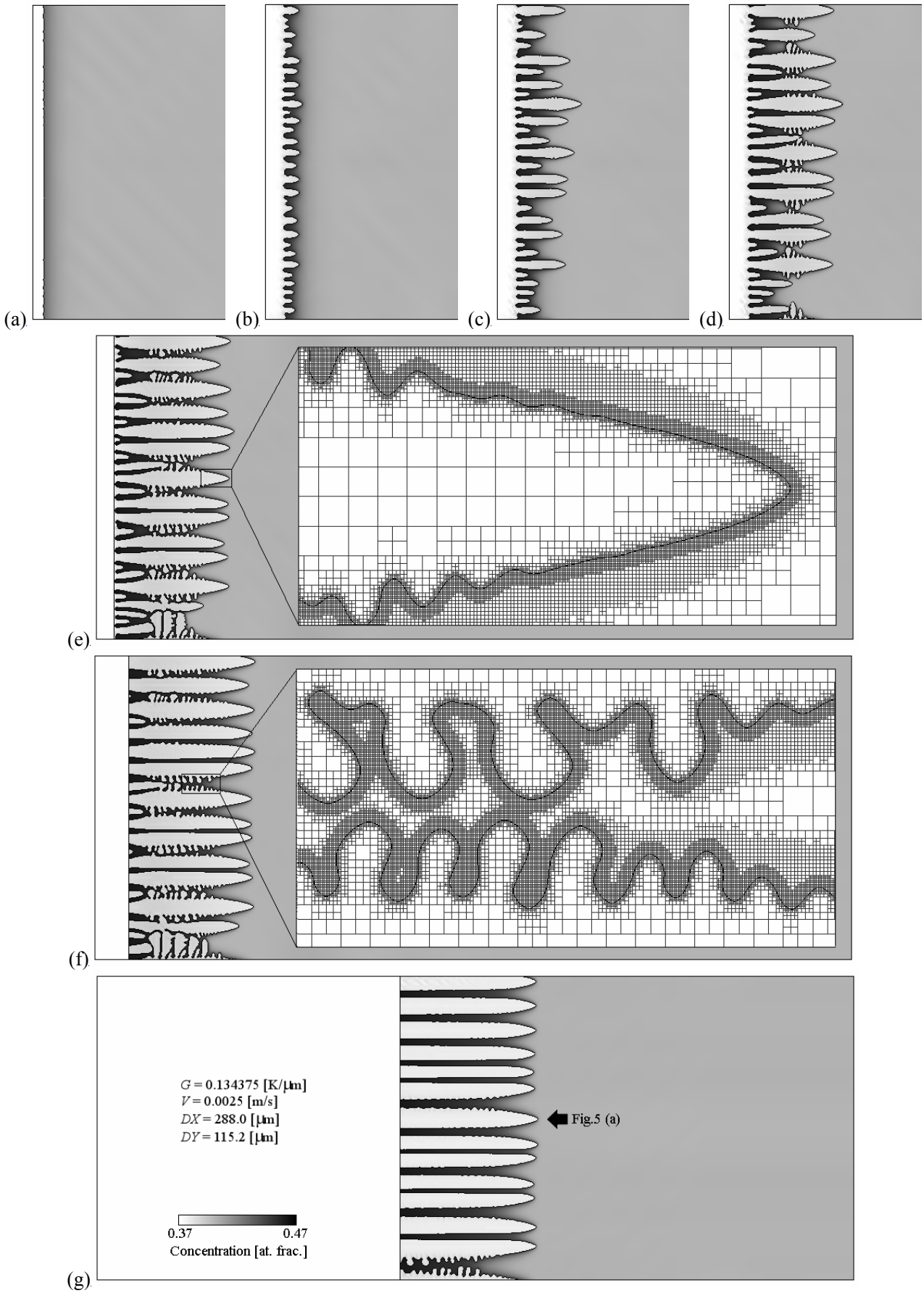

Fig.4 Time evolution of interface (solid black line) and concentration field. Step numbers are (a) 32000, (b) 57600, (c) 62080, (d) 64000, (e) 66560, (f) 69120, and (g) 110080, which correspond to time because dt = 1 μs.

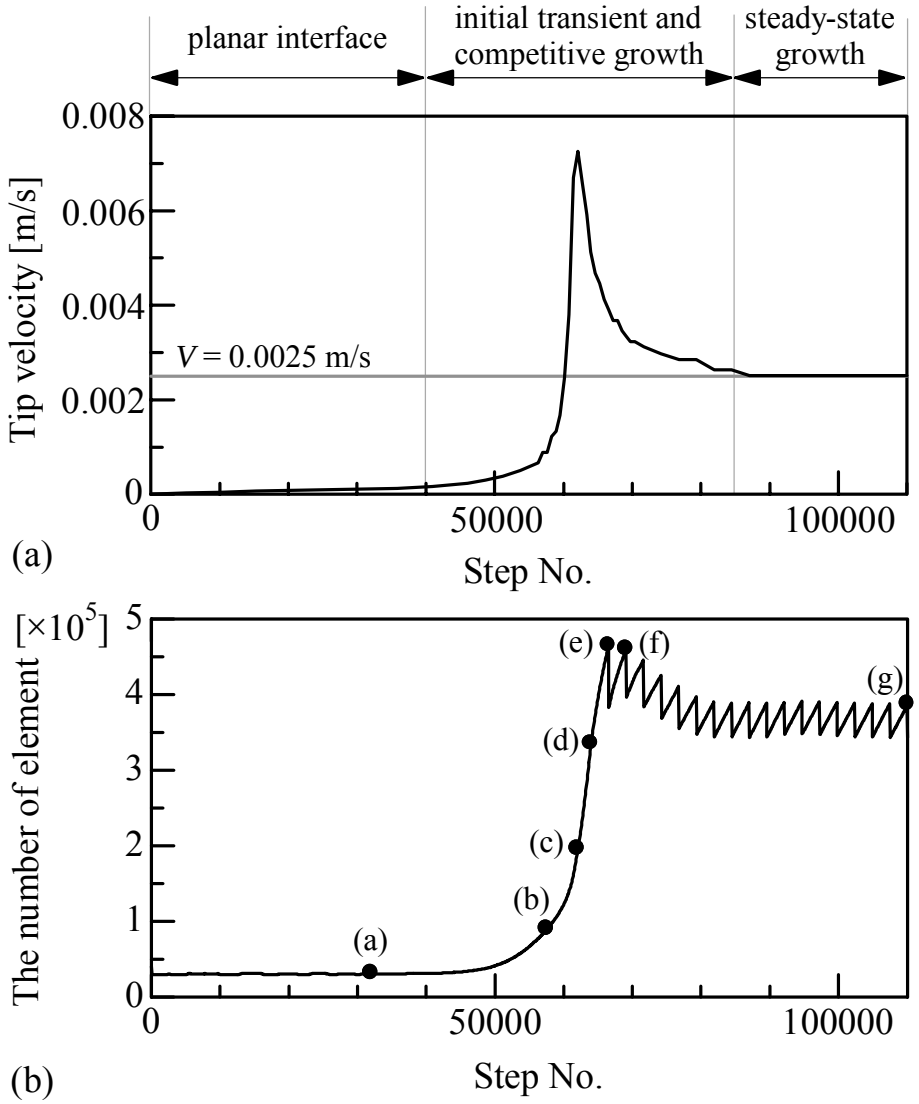

Fig.5 Variations of (a) tip velocity of cell indicated by arrow in Fig.4 (g) and (b) total number of active elements in the simulation shown in Fig.4.

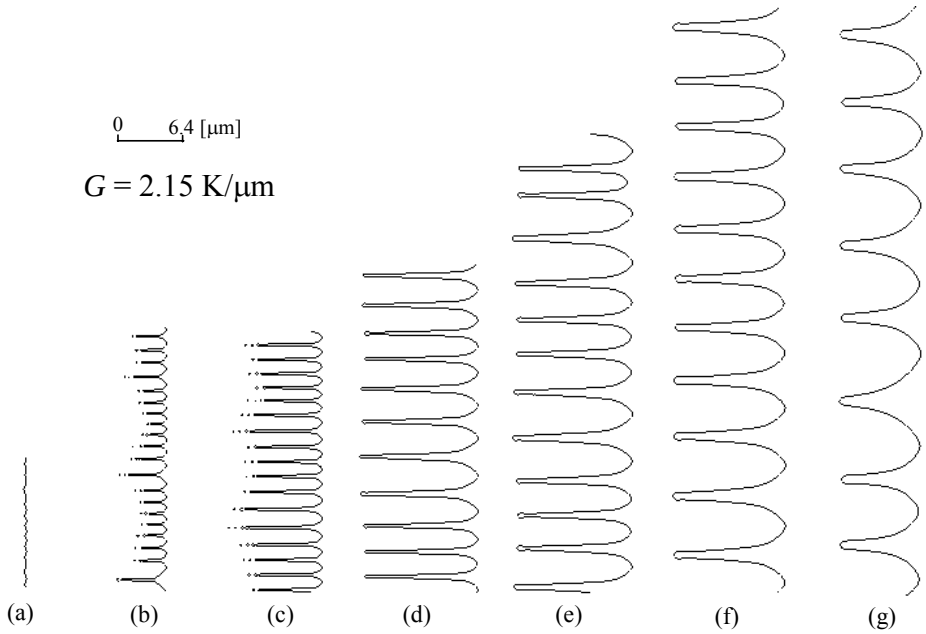

Fig.6 Effects of pulling velocity on the steady-state cellular structures. V = (a) 0.02, (b) 0.01, (c) 0.005, (d) 0.0025, (e) 0.00125, (f) 0.000625, and (g) 0.0003125 m/s.

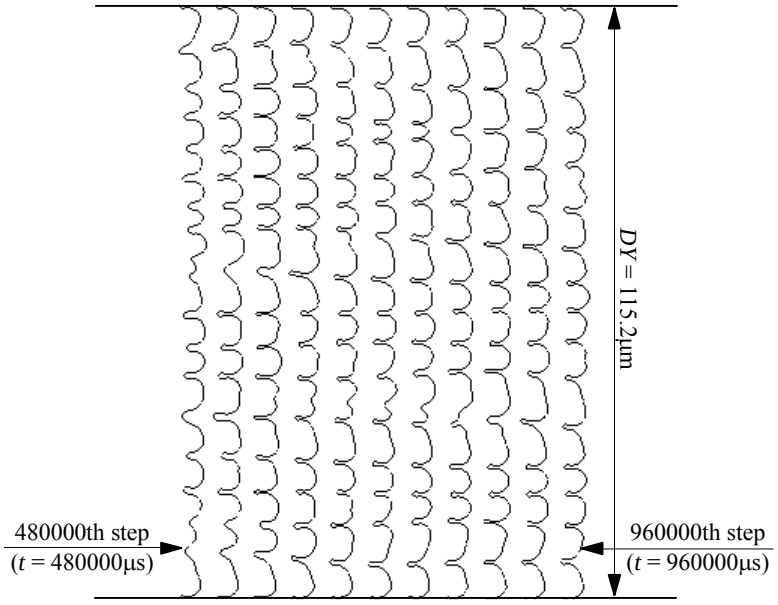

Fig.7 Interface morphologies every 48000 steps from 480000th step to 960000th step for V = 0.00015625 m/s.

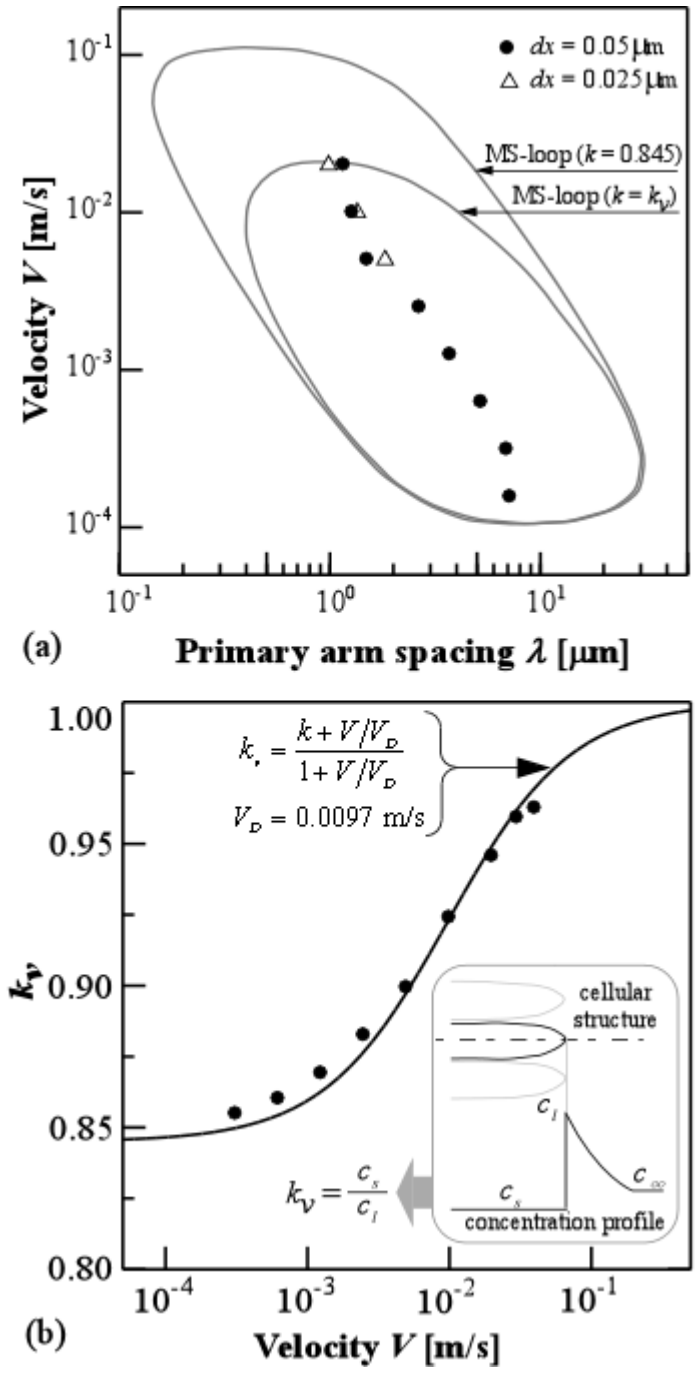

Fig.8 Plots of (a) V and λ, and (b) k_v and V.

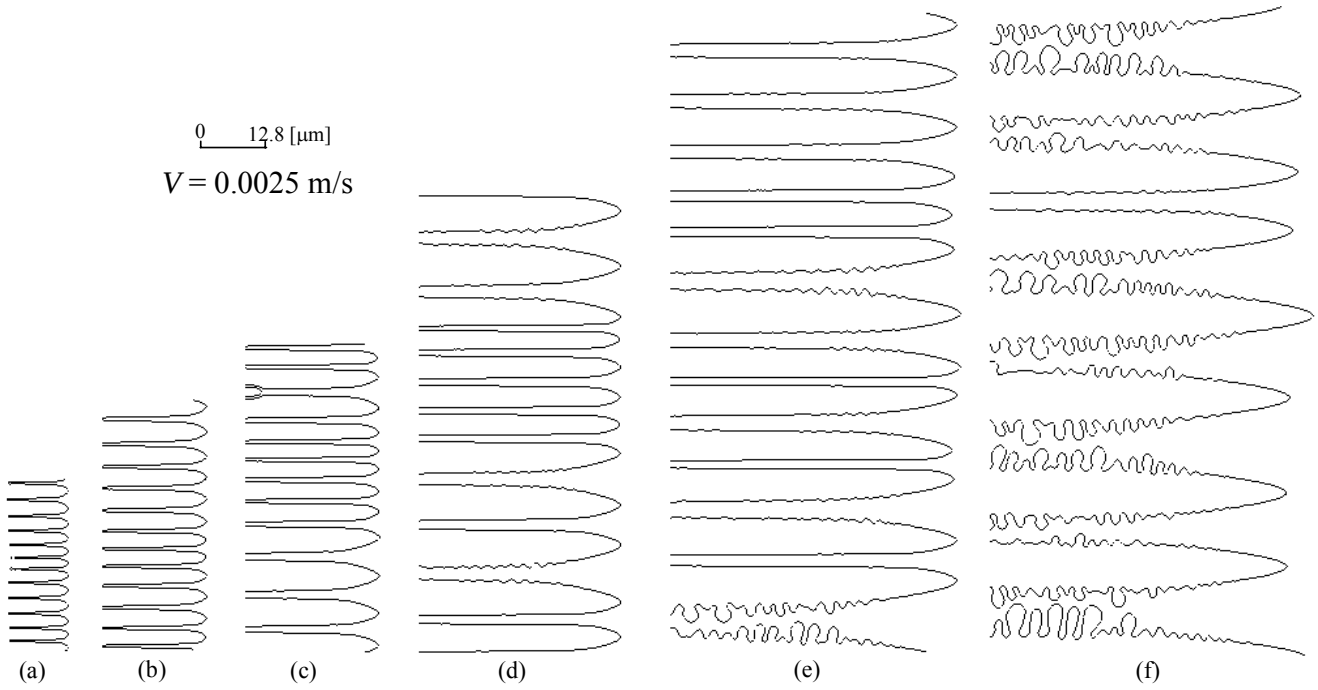

Fig.9 Effects of temperature gradient on the steady-state interface morphology. G = (a) 2.15, (b) 1.075, (c) 0.5375, (d) 0.26875, (e) 0.134375, and (f) 0.0671875 K/μm.

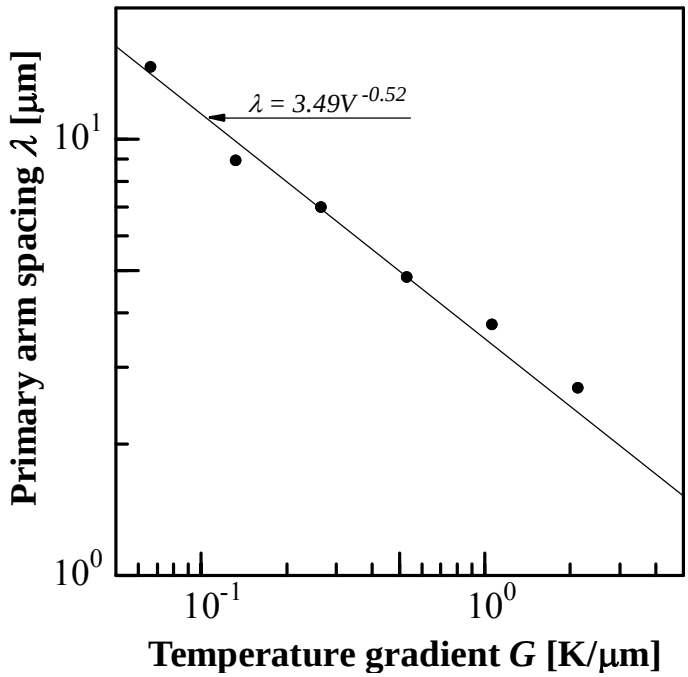

Fig.10 Plot of λ and G

Table.1 Numerical conditions and results under constant value of G = 2.15 K/μm.

V [m/s]	DX [μm]	DY [μm]	t_{total} [μs]	N	λ [μm]
0.04	96.0	12.8	3800	planar	–
0.03	96.0	12.8	3800	planar	–
0.02	96.0	12.8	3800	11	1.164
0.01	96.0	25.6	7500	20	1.280
0.005	96.0	25.6	15000	17	1.506
0.0025	96.0	32.0	30000	12	2.667
0.00125	96.0	44.8	60000	12	3.733
0.000625	96.0	57.6	120000	11	5.236
0.0003125	96.0	83.2	240000	12	6.933
0.00015625	288.0	115.2	960000	16	7.200
0.000078125	576.0	160.0	1920000	planar	–

Table.2 Numerical conditions and results under constant value of V = 0.0025 m/s.

G [K/μm]	DX [μm]	DY [μm]	t_{total} [μs]	N	λ [μm]
2.15	96.0	32.0	30000	12	2.667
1.075	192.0	44.8	64000	12	3.733
0.5375	192.0	57.6	64000	12	4.800
0.26875	192.0	83.2	64000	12	6.933
0.134375	288.0	115.2	128000	13	8.862
0.0671875	384.0	160.0	148480	11	14.545